Nanoscale

PAPER

View Article Online
View Journal | View Issue

Cite this: *Nanoscale*, 2017, **9**, 19346

Unprecedented sensitivity towards pressure enabled by graphene foam†

Xiaoling Zang,‡[a,b,c] Xusheng Wang,‡[d] Zhanhai Yang,[a,c] Xiaowei Wang,[b] Rui Li,[e] Jitao Chen,[d] Junhui Ji[b] and Mianqi Xue *[a]

Received 16th July 2017,
Accepted 16th November 2017

DOI: 10.1039/c7nr05175a

rsc.li/nanoscale

Reduced graphene oxide foam (RGOF)-based pressure sensors have been fabricated through the combination of ultrasonic dispersion and freeze-drying methods. Due to the maintenance of the highly disordered structure of the ultrasonic dispersed graphene oxides before the freezing process, the RGOF sensors demonstrated an ultra-high sensitivity of 22.8 kPa^{-1}, an ultra-low detection limit of around 0.1 Pa, and a superior separation of 0.2-Pascal-scale difference.

1. Introduction

After several years of rapid development, pressure sensors,[1,2] which are based on the linkage electrical shift and mechanical deformation,[3] have attracted much attention due to their bright prospects in the fields of artificial organs,[4] wearable devices,[5] touch-on flexible displays,[6] soft robotics,[7] and health monitoring systems.[8] Besides the miniaturization, flexibility, stretchability, wearability, and integration of smart sensors,[9–11] tremendous efforts have been devoted to the improvement of the sensitivity and detection limit.[12–33] In this context, seeking the suitable measuring principles, preferable sensing materials, and cost-effective methods is essential to the practical application of sensors. Pressure induced changes in the electrical resistance, piezoelectricity, capacitance, potential and other detectable signals have been used for fabricating different types of pressure sensor.[13] Conductive polymers,[14] semiconducting nanowires,[15] metal nanowires,[16] carbon nanotubes,[17] and especially graphene[18] have been developed as sensing materials. Meanwhile, the dip-coating[19] and electro- and electroless-plating processes,[20,21] soft lithography,[22–25] drop casting,[26] electrospinning,[27] direct writing,[28,29] and other bottom-up approaches[16,30] have been applied to next-generation pressure sensors. However, the ultimate pursuit of a pressure sensor, detecting ultra-low pressure with a strong output signal, is still the primary limitation.

As a widely accepted strategy, the vesiculation of the sensing materials,[34] especially graphene-based materials,[35] has recently attracted considerable attention in solving this problem. Generally, driven by the surface activity of the graphene or graphene oxide nanofilm, graphene foam (GF) and its congeners (sponges and aerogels),[36–38] can be synthesized with high electrical conductivity and elasticity *via* different strategies, such as freeze drying,[39] controlled reassembly,[40] hydrothermal reduction,[41] and chemical vapor deposition (CVD).[42] To date, along with these fast-developed techniques, graphene and GF open a vast and applicable foreground in the fields of energy storage,[39,41,43] oil–water separation,[44] environment monitoring,[45] superconductors,[46,47] and smart sensors.[48–50] Owing to its intrinsic characteristics, including its typical porous structure, high electrical conductivity, and outstanding elasticity, GF is considered to be one of the best choices for fabricating resistance-type pressure sensors. For example , Yu's team has fabricated a fractured graphene-wrapped polyurethane (PU) sponge with high flexibility, which can detect pressure as low as 9 Pa and has a sharp output signal at a pressure of 45 Pa (the sensor possesses a sensitivity of 0.26 kPa^{-1} and high stability over 10 000 cycles).[48] Commercially available PU foam was used by Samad and co-workers as a template for fabricating freestanding GFs with tunable densities and adjustable shapes and sizes, and the different density GFs exhibited different sensitivities to the applied pressure.[49] Most recently, Wan *et al.* succeeded in fabricating a graphene oxide (GO) foam with excellent elasticity and they also presented a GO-based sensor with a subtle pressure of ~0.24 Pa and a sensitivity of 0.8 kPa^{-1}.[50]

Despite being one kind of the ideal sensing materials, these different types of GF are still restricted by their unsatis-

[a]*Institute of Physics and Beijing National Laboratory for Condensed Matter Physics, Chinese Academy of Sciences, Beijing 100190, China. E-mail: xuemq@iphy.ac.cn*
[b]*Technical Institute of Physics and Chemistry, Chinese Academy of Sciences, Beijing 100190, China*
[c]*University of Chinese Academy of Sciences, Beijing 100049, China*
[d]*Beijing National Laboratory for Molecular Sciences, College of Chemistry and Molecular Engineering, Peking University, Beijing 100871, China*
[e]*School of Advanced Materials, Peking University Shenzhen Graduate School, Shenzhen 518055, China*

†Electronic supplementary information (ESI) available. See DOI: 10.1039/c7nr05175a

‡These authors contributed equally to this work.

factory sensitivity. Generally, the sensitivity of the GF is determined by the size and distribution of the pores in the foam, the thickness of the pore walls, and the density.[51] Obviously, the degree of disorder is the crucial influence on the pressure-response output signals when the thickness and the density are essentially unchanged. Therefore, wide interest has been stimulated to develop new feasible methods for preparing GFs with satisfactory disorder to fabricate high-performance pressure sensors with satisfactory sensitivities, detection limits, response times, and stabilities. Unlike the current methods for fabricating GFs (the initial method was to coat GO nanosheets onto the backbone of a PU sponge through solution dipping,[48] a further method of thermal annealing a GO-coated-PU foam was developed,[49] and the recent approach was the direct freeze drying of a GO solution[50]), here we introduce an ultrasonic dispersion method to build highly disordered reduced graphene oxide foams (RGOFs) without any additives. The structure is maintained by the freeze-drying process.[52] The as-fabricated RGOF-based pressure sensor exhibits an unprecedented sensitivity of up to 22.8 kPa^{-1} and an ultralow detection limit of around 0.1 Pa. These results could rank as top among the published best-performing sensors. Furthermore, the RGOF-based pressure sensor could be used for monitoring even very small changes in human motion.

2. Results and discussion

A GO aqueous dispersion was prepared by a modified Hummers method. In order to obtain statistical information about the GO sheets, atomic force microscopy (AFM) was performed (Fig. S1, ESI†). The lateral sizes ranged from hundreds of nanometers to tens of micrometers, and the thicknesses ranged from ~0.49 nm to less than 3.0 nm. According to the statistical counts of the thicknesses of each sample, we can conclude that approximately 100% of the as-fabricated products were few-layer 2D sheets (<10 layers).

The typical procedure used for fabricating the RGOF is illustrated in Fig. 1. Firstly, the GO aqueous dispersion was prepared by ultrasonication in cold water. Due to the three-dimensional effect of ultrasound, this step resulted in the highly disordered structure of the GO sheets. Then the GO aqueous dispersion was frozen under −80 °C to maintain the highly disordered structure. The following freeze-drying step removed the water solvent in the voids and avoided collapse of the structure. To obtain the RGOF (with reduced graphene oxide as the building block), the prepared GO foam (GOF) was reduced in Ar/H_2 atmosphere, which could keep the highly disordered structure intact.

The scanning electron microscopy (SEM) analyses of the GOF and RGOF are displayed in Fig. 2a and b. Both of them reveal the interconnected sheets with disordered configuration and the open porous morphology with variable pore size. Thus, the reduction process did not damage the disordered structure. Compared with the previously reported familiar GFs with quasi-honeycomb structures,[48–50] the as-fabricated RGOF is in a state of almost complete disorder. Furthermore, despite the disordered arrangement of the rGO sheets, the interlocking network in the RGOF provides elasticity and flexibility in the sensing field (the real-time images of the compression–recovery process are shown in Fig. S2 (ESI†)). The H_2 species in the Ar atmosphere could significantly eliminate the oxygenic groups (such as C–O, C═O, and O–C═O) in GOF. As shown in Fig. 2c and d, the energy-dispersive X-ray (EDX) spectroscopy elemental mapping images of the GOF and RGOF were recorded and the corresponding SEM images are exhibited in Fig. S3 (ESI†). The intuitive comparison of the dots distribution indicates a decrease of the O element in the RGOF, and the molar ratios of the C and O elements for the GOF and RGOF are separately simulated to be 1.6 and 14.4, respectively. Thus, the RGOF has a high-level reduction of the oxygenic

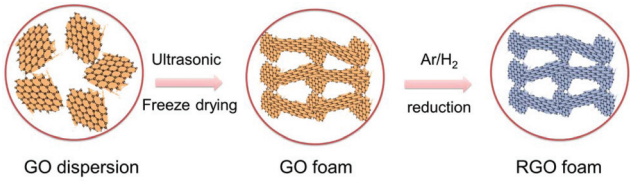

Fig. 1 A schematic of the fabrication process of the RGOF. The ultrasound step with three-dimensional effect could provide the highly disordered structure for the GO sheets in aqueous dispersion under a cold environment. The freezing step under −80 °C could maintain the highly disordered structure of the GO sheets. Then the freeze-drying step removed the solvent and protected the highly disordered structure. The last reduction process could decrease the oxygenic groups and keep the highly disordered structure intact.

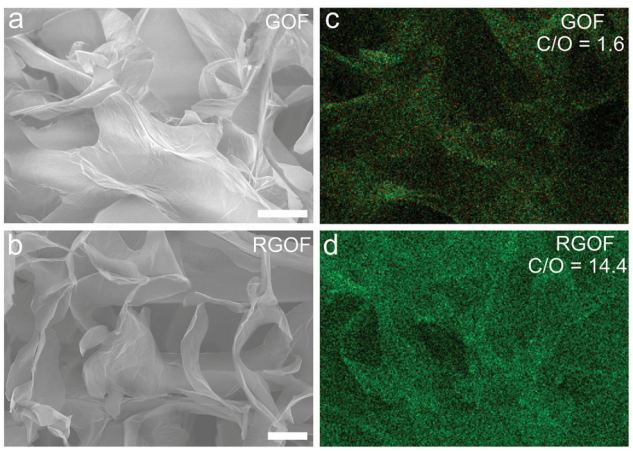

Fig. 2 The structural and morphological characterizations of the GOF and RGOF. (a) The SEM image of the GOF. It presents the interconnected sheets with disordered configuration and the open porous morphology with variable pore size. (b) The SEM image of the RGOF. It shows a highly disordered structure and has no obvious changes compared to the GOF. (c, d) The EDX images of the GOF and RGOF. The dots distribution manifests that the content of the O element in the RGOF diminishes obviously compared to that of the GOF, and the molar ratios of the C and O elements are severally fitted to be 1.6 and 14.4 for the GOF and RGOF. The scale bars in panels (a) and (b) are both 20 μm.

groups, which is favourable for the improvement of the electrical conductivity.

The surface chemical states of the GOF and RGOF were analyzed by means of X-ray photoelectron spectroscopy (XPS). In Fig. 3a, the survey spectrum of the GOF reveals an intensive O 1s peak, indicating the enrichment of the oxygenic groups. Yet in Fig. 3b, the O 1s peak intensity in the survey spectrum of the RGOF demonstrates a sharp decrease, which is consistent with the results of EDX spectroscopy. For the C 1s region of the GOF illustrated in Fig. 3c, the peak-fitting deconvolution exhibits one carbon-related peak at 284.6 eV, corresponding to graphitic structure (C–C and C═C bonds), and three oxygen-related peaks at 285.3, 288.4, and 291.0 eV, corresponding to hydroxy C–O, carbonyl C═O, and carbonyl O–C═O bonds, respectively.[53,54] In striking contrast, the oxygenic groups in the C 1s region of RGOF (Fig. 3d) decrease obviously, which should be attributed to the reduction process. The C/O ratios of the GO and rGO foams are simulated to be 1.7 and 14.8, respectively, from the XPS data. In Fig. S4a (ESI†), the Fourier transform infrared (FTIR) spectroscopies of the GOF and RGOF are presented. Compared to the GOF, the most obvious change in the RGOF is the disappearance of the O–H bond. The C–O and C═O bonds are also diminished,[55] which is in accordance with the XPS spectra. To consolidate the characterizations of the GOF and RGOF, the Raman spectra were also collected. As displayed in Fig. S4b (ESI†), the intensity ratio of the D (1350 cm^{-1}) and G (1590 cm^{-1}) peaks (I_D/I_G) for the GOF is fitted to be 0.94, whereas this ratio is 1.02 for the RGOF with the almost unchanged peak positions (1350 and 1594 cm^{-1} for the D and G peaks, respectively). This manifests the increase of the sp^2 domains and the more disordered structure in the RGOF.[54]

The production process of the RGOF-based sensor device and the corresponding schematic are displayed in Fig. S5 and S6 (ESI†), respectively (the details are supplemented in the Experimental section). The sensitivity of the RGOF sensor with a diameter of 4.5 cm was investigated. The initial thickness is around 2 mm. Fig. 4a shows the pressure response from both the RGOF sensor and the rGO-sheet-based pressure sensor (the production details are supplemented in the Experimental section). The sensitivity S can be defined as:[51]

$$S = \delta(\Delta R/R_0)/\delta p,$$

where R_0 is the resistance before applying pressure and p is the pressure applied. ΔR is the difference between R_0 and the resistance with pressure applied, R_p. δ has the same meaning as Δ in this formula. As shown in Fig. 4a, there are two different pressure sensitivities in the low- and high-pressure regions. The RGOF sensor shows an ultra-high sensitivity as high as 22.8 ± 1.3 kPa^{-1} in the low-pressure region from 0 to 10 Pa. Obviously, such a RGOF sensor can solve the detection fatigue of the ultra-slight changes of pressure or human motion, whereas previously reported pressure sensors almost always focus on 10 Pa- or kPa-scale detection. The rGO-sheet-based pressure sensor, by contrast, can only detect pressure above 100 Pa, and the sensitivity is close to that of the RGOF sensor (1.34 ± 0.17 kPa^{-1}) at higher pressures. These results are among the best performances published for pressure sensors, and the sensitivity of 22.8 kPa^{-1} is two or three orders of magnitude higher than previously reported graphene-based pressure sensors.

In further study of the sensing behaviors of the RGOF sensors, the change of the electrical resistance *versus* ultra-low pressures, continuous detection, and working stability were

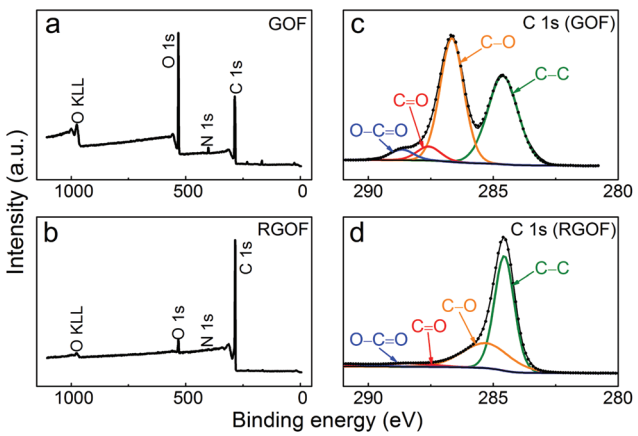

Fig. 3 The XPS curves of the GOF and RGOF. (a) The survey spectra of the GOF. The intensive O 1s peak indicates the enrichment of the oxygenic groups in the GOF. (b) The survey spectra of the RGOF. Compared to the GOF, the content of the O element decreases dramatically in the RGOF. (c) The C 1s region of the GOF. The graphitic structure C–C and C═C , hydroxy C–O, and carbonyl C═O and O–C═O bonds are detected in the GOF. (d) The C 1s region of the RGOF. Compared to the GOF, the oxygenic groups in the RGOF decrease obviously, which is consistent with the results of the EDX images.

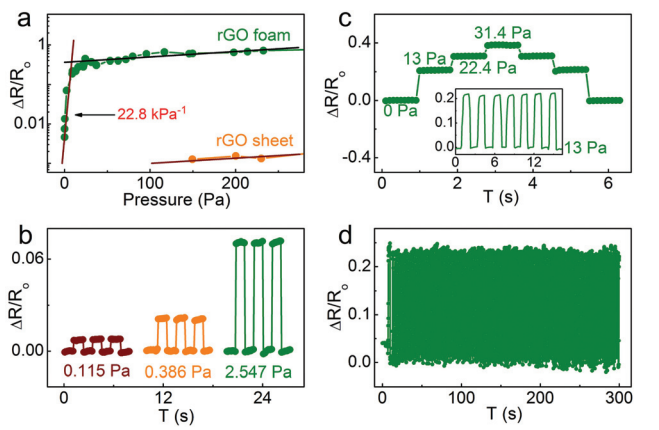

Fig. 4 (a) The pressure-response curve for the RGOF sensor and rGO sheet-based pressure sensor. The sensitivity is 22.8 kPa^{-1} in the low-pressure region from 0 to 9.5 Pa. (b) The change of electrical resistance ($\Delta R/R_0$) *versus* ultra-low pressures, even down to 0.1 Pa. The response time is 100 ms. (c) The sensing behaviour of the RGOF sensor towards different pressures of 13, 22.4 and 31.4 Pa. Inset: The resistance variation ratio recorded in the seven 13 Pa-loading/unloading cycles. (d) The working stability of the RGOF sensor for the first 120 cycles under a pressure of 13 Pa.

investigated. As shown in Fig. 4b, the RGOF sensor has a high differentiation of 0.26 Pa, while the detection limit is down to the 0.1 Pa scale. Meanwhile, the response time is around 100 ms. Furthermore, continuous tests of the RGOF sensor towards the different ultra-low pressures of 13, 22.4 and 31.4 Pa have been conducted to further evaluate the sensing performances. Fig. 4c shows a positive correlation between $\Delta R/R_0$ and the external pressure. The change of electrical resistance induced by various external pressures can be clearly distinguished and exhibits excellent recovery capability. Meanwhile, the resistance variation ratio of the seven 13 Pa/0 Pa cycles is shown in the inset of Fig. 4c. The $\Delta R/R_0$ value is around 0.2 and remains stable in each cycle with consistent fluctuation. Additionally, the working stability of the RGOF sensor was tested by loading/unloading 13 Pa for more than 5000 cycles (Fig. 4d and Fig. S7, ESI†). Fig. 4d shows the tiny change of the resistance variation ratio in the stability test, and the change of the sensitivity is less than 2%. Both Fig. 4c and d demonstrate the excellent working stability of such RGOF sensors.

Fig. 5a and b both illustrate the detection of the pressing and bending forces at room temperature. As seen from Fig. 5a, the obvious changes of resistance in the several press/release cycles demonstrate favorable reproducibility on one hand and sharp embossing (fast response) on the other. In addition, very slight bending (in the inset in Fig. 5b, the simulated bending radius of the foam is 341 mm) has also been detected using the RGOF sensor. In Fig. 5b, the result exhibits outstanding responsiveness and stability. In the case of these tests, the press/release and bend/release curves are very symmetrical and sharp, indicating excellent recovery property. With the excellent sensing performances in sensitivity, detection limit, response time and stability, the RGOF sensor can be applied to detect a full range of human motions. Fig. 5c exhibits the notable resistance changes of the RGOF sensor with very slight finger shifts. Different imperceptible finger movements (as the inset shows in Fig. 5c, the simulated maximum bending radius of the foam is 128 mm) can be easily reflected by the changes in the relative resistance of the RGOF sensor. Compared with the rGO sheet-based pressure sensor, the RGOF sensor presents an enormous enhancement in the tiny-movement sensing aspect (nearly tens of times), and its signals change more obviously than those of other sensors.

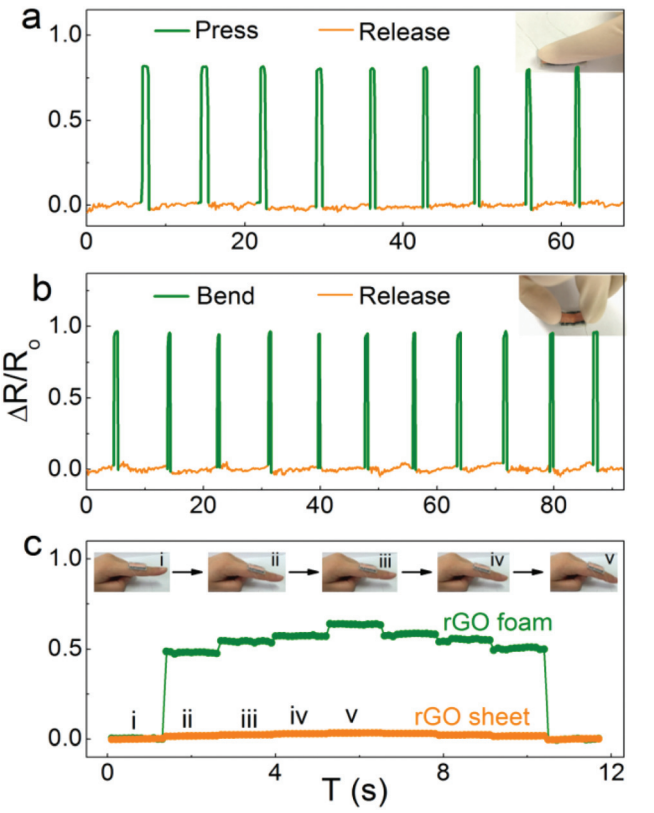

Fig. 5 (a, b) The application of the RGOF sensor in detecting the pressing (a) and bending (b) forces. (c) The sensing behavior of the RGOF sensor and rGO sheet-based pressure sensor towards very slight finger movements. The inset shows the corresponding states of the finger movements.

The ultra-high sensitivity (22.8 ± 1.3 kPa^{-1}) in the low-pressure region from 0 to 10 Pa (the resistive variation of 7% can be detected under a pressure of 2.54 Pa), the ultra-low detection limit (the resistive variation of 0.9% can be detected under a very low pressure of 0.11 Pa) and the fast response time (100 ms) make the RGOF sensors very suitable for application in the fields of electronic skin and smarter robots. In fact, 3D graphene-based materials with various structures such as nanopapers,[56] sponges,[48] and foams,[57] have been considered very recently as promising components for piezoresistive sensors owing to the combination of 3D porous structures, excellent electrical conductivities, and compressive elasticities.[51] Indeed, the pressure-sensing mechanism is determined by the change of the ordering degree. The structure of the RGOF changes from the completely disordered state to the preferable ordered one during compression, and then back to the original disordered state after the release. The contact resistance between the adjacent rGO nanosheets varies obviously in the compression/release cycles, appearing as the sensitive pressure-resistance response. The diminishing degree of disorder is confirmed in the order of the initial RGOF, the compressed RGOF after a long-term cycling test with large pressure (≥300 Pa), and the initial RGO sheets (Fig. S8, ESI†). After the long-term cycling test with high pressure, the high degree of disorder in the RGOF would suffer some irreversible damage, thus destroying the reproducibility within the small pressure-test range. Hence, in the premise of maintaining the elasticity of the RGOF (here P should not be more than 300 Pa), the freeze of the highly disordered structure of the ultrasonic dispersed graphene oxides in this design brings out the superb sensing performances. During the freezing process, the plentiful nanogaps between the graphene nanosheets in the wall of the micropore are preserved, which provides ultra-high sensitivity ($S \sim 22$ kPa^{-1}) in the very low-pressure region (0–10 Pa). Furthermore, the micropores are deformed gradually with the added pressure (>10 Pa), offering the second region of the pressure-resistance response (~1.3 kPa^{-1}). The sensing per-

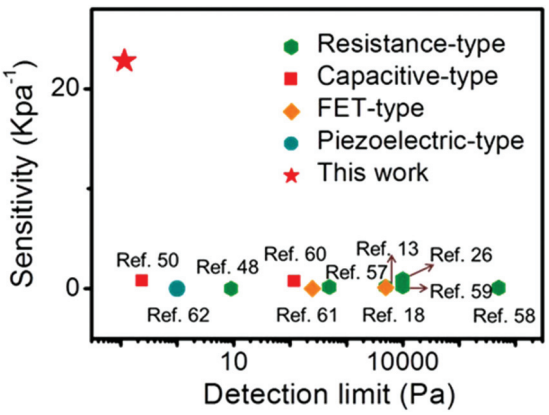

Fig. 6 The comparison of the RGOF sensor to other reported graphene-based pressure sensors.

formances of the RGOF sensors are compared to some previously reported pressure sensors and plotted in Fig. 6.[13,18,26,48,50,51,57–62] The ultra-high sensitivity of the RGOF sensor is higher than previous graphene-based pressure sensors, whether these were resistance-type devices (0.03–1.61 kPa^{-1}),[13,26,48,51,57–59] capacitive-type devices (0.73–0.8 kPa^{-1}),[50,60] FET-type devices (2.05 × 10^{-4}–0.12 kPa^{-1})[18,61] or piezoelectric-type devices (9.4 × 10^{-3} kPa^{-1}).[62] More importantly, an obvious resistance variation can be detected under a very low pressure of 0.11 Pa. Hence, the electrical conductivity of the RGOF is very sensitive to the pressure. The ultra-low detection limit and fast response time make it very competitive for electronic artificial skin and highly sensitive pressure sensors.

3. Experimental

Synthesis of the GO dispersion

2 g of expanded graphite was added to a dry 1000 mL beaker, then 92 g of concentrated sulfuric acid was slowly poured into the beaker, which was then sealed with a sealing film. After being stirred for 24 h at a speed of 200 rpm, 1 g of $NaNO_3$ was added to the beaker under stirring for 5 min. Then 6 g of $KMnO_4$ was very slowly added to the beaker at ~0 °C (in an ice bath) and stirred for 5 min. The beaker was then transferred into a water bath (35 °C) and stirred for 30 min. After stopping the water bath, 5 mL of water was added to the beaker along the wall and stirred for 5 min. Then 5 mL of water was again added along the wall. After 5 min, 40 mL of water was added to the beaker and stirred at a speed of 350 rpm for 30 min. Then 400 mL of water was added to the beaker and kept stirring at the speed of 750 rpm for 5 min. After that, 20 mL of H_2O_2 (35%) was added to the beaker and kept stirring for 5 min. After stopping stirring, the natural settlement of the dispersion was allowed for 2 h. Then the supernatant was removed and the dispersion left was washed with hydrochloric acid solution. The washing process was repeated again. Then the GO dispersion was obtained by centrifugation process.

Preparation of the RGOF and rGO sheet samples

The GO aqueous dispersion (3 mg mL^{-1}; 15 mL) was treated with ultrasound in cold water (below 10 °C, SB-5200DTDN, 100 W, 40 kHz) for 1 h. After that, it was frozen at −80 °C for 2 h. The sample was then freeze-dried for 40 h and reduced at 800 °C for 6 h under Ar/H_2 atmosphere (H_2 is 5 vol%) to obtain the RGOF, which was a round shape with a diameter of 45 mm. After the freeze-drying process, the GO foams were pressed into flexible films and then reduced at 800 °C for 6 h under Ar/H_2 atmosphere (H_2 is 5 vol%) to obtain the rGO sheet samples.

Material characterizations

The atomic force microscopy (AFM) images of the GO sheets were recorded with a Dimension 3100. The morphological, elemental-mapping, and microstructural characterizations of the GOF and RGOF were visualized by scanning electron microscopy (SEM, S4800, Hitachi). The elemental analyses were performed by X-ray photoelectron spectroscopy (XPS, Axis Ultra, Kratos Analytical Ltd). The Fourier transform infrared (FTIR) spectra of the GOF and RGOF were collected by a Nicolet 6700 FTIR system. The Raman spectra of the GOF and RGOF were recorded using a Raman spectrometer (ARAMIS, HORIBA Jobin Yvon, 532 nm excitation wavelength, laser power is 13 mW).

Preparation of the RGOF- and rGO sheet-based sensor devices

First, the diluted silver paste was uniformly coated on one surface of the copper foil, and the prepared RGOF was placed on this surface of the copper foil. After the silver paste was fully cured, the other copper foil coated with silver paste was capped onto the top surface of the RGOF, two wires were separately fixed onto the surfaces of the two copper foils by silver paste, and the RGOF-based sensor device was prepared. The rGO sheet-based sensor device was prepared by a similar process. Before the preparation of the RGOF-based sensor device, a stainless steel block (Fig. S2a, ESI†) was used to compress the RGOF one time to avoid the interface effect and ensure data reproducibility.

Sensing tests of the RGOF- and rGO sheet-based sensor devices

Two aluminium wires were separately glued to the inner surfaces of the upper and lower copper foils, and then they were connected with the test instrument. The pressure sensing tests were measured on a Keithley 2400 at the given voltages of 0.1, 0.5, and 1.0 V. The given voltage of 0.1 V could be used to conduct the entire sensing test, and the voltages of 0.5 and 1 V were adopted to compare with the results of 0.1 V. During the test, various pressures from 0.1 to 300 Pa were put on the RGOF sensor and the resistance change response was recorded. Within the range of smaller pressure, the low-density and low-weight plastic foams were used as the pressure sources (Fig. S9 and Video 1, ESI†). The bigger pressure was continuously provided by the pressure measuring instrument

(HANDPI-HP Digital Force Gauge). The RGOF with a size of 15 × 10 mm^2 was assembled into a resistive-type pressure sensor by the above sandwiching method and fixed by Scotch tape. Then the resistive-type pressure sensor was used as a wearable pressure sensor to monitor the finger bending and finger movement by attaching the sensor onto a person's finger joint.

4. Conclusions

In summary, we report a novel and low-cost strategy to fabricate a graphene-based highly-sensitive pressure sensor through the combination of ultrasonic dispersion and freeze-drying methods. The ultrasonic dispersion method is used to realize a high degree of disorder, and furthermore the highly disordered structure can be preserved in the freeze-drying process. The as-fabricated RGOF with a state of almost complete disorder is quite different to the previously reported GFs with quasi-honeycomb structures.[38–40] Due to the maintenance of the highly disordered structure, the flexible RGOF sensor exhibits ultra-high sensitivity at very low pressure, a fast pressure response, and excellent cycling stability. Specifically, to the best of our knowledge, the ultra-high sensitivity (~22.8 kPa^{-1}), the limit of detection down to 0.11 Pa, and the superior separation of 0.2-Pascal-scale difference are among the reported highest-performance graphene-based pressure sensors.

Meanwhile, the RGOF sensor can even monitor very small human motions (such as finger bending with very small radius) accurately and sensitively. Therefore, these performances, incorporating ultra-high sensitivity, ultra-low detection limit, and fast response and simultaneously combining the advantages of being freestanding, flexible, low cost and having simplicity in device fabrication, mean that the RGOF sensor has many potential applications, such as artificial skin, wearable sensors, health monitoring platforms, and even further multi-functional (such as thermal, chemical, and biological) integrated sensing systems.

Conflicts of interest

There are no conflicts to declare.

Acknowledgements

The authors wish to thank F. Li, Dr X. Ma, Prof. G. Chen, and Z. Ren for their discussion and support. This work was supported by the National Natural Science Foundation of China (21622407, 21673008, 21404009), the National Key Research and Development Program of China (2016YFB0700604), the Shenzhen Science and Technology Research Grant (JCYJ20160531141109132, JCYJ20170412150450297), and Guangdong Innovative and Entrepreneurial Research Team Progress (2013N080).

References

1 T. Someya, T. Sekitani, S. Iba, Y. Kato, H. Kawaguchi and T. Sakurai, *Proc. Natl. Acad. Sci. U. S. A.*, 2004, **101**, 9966–9970; C. S. Boland, U. Khan, G. Ryan, S. Barwich, R. Charifou, A. Harvey, C. Backes, Z. Li, M. S. Ferreira, M. E. Möbius, R. J. Young and J. N. Coleman, *Science*, 2016, **354**, 1257–1260.
2 G. Schwartz, B. C. Tee, J. Mei, A. L. Appleton, D. H. Kim, H. Wang and Z. Bao, *Nat. Commun.*, 2013, **4**, 1859.
3 M. L. Hammock, A. Chortos, B. C. K. Tee, J. B. H. Tok and Z. Bao, *Adv. Mater.*, 2013, **25**, 5997–6038.
4 D.-H. Kim, N. Lu, R. Ma, Y.-S. Kim, R.-H. Kim, S. Wang, J. Wu, S. M. Won, H. Tao, A. Islam, K. J. Yu, T.-I. Kim, R. Chowdhury, M. Ying, L. Xu, M. Li, H.-J. Chung, H. Keum, M. McCormick, P. Liu, Y.-W. Zhang, F. G. Omenetto, Y. Huang, T. Coleman and J. A. Rogers, *Science*, 2011, **333**, 838.
5 C. Pang, C. Lee and K.-Y. Suh, *J. Appl. Polym. Sci.*, 2013, **130**, 1429–1441.
6 C. Wang, D. Hwang, Z. Yu, K. Takei, J. Park, T. Chen, B. Ma and A. Javey, *Nat. Mater.*, 2013, **12**, 899–904.
7 N. Lu and D.-H. Kim, *Soft Robot.*, 2014, **1**, 53–62.
8 A. Pantelopoulos and N. G. Bourbakis, *IEEE Trans. Syst. Man Cybern. Part C*, 2010, **40**, 1–12.
9 M. Xue, X. Ma, Z. Xie, L. Duan, Y. Jiang, M. Zhang and T. Cao, *Chem. – Asian J.*, 2010, **5**, 2266–2270.
10 M. Xue, F. Li, Y. Wang, X. Cai, F. Pan and J. Chen, *Nanoscale*, 2013, **5**, 1803–1805.
11 M. Xue, Y. Wang, X. Wang, X. Huang and J. Ji, *Adv. Mater.*, 2015, **27**, 5923–5929.
12 M. Xue, F. Li, D. Chen, Z. Yang, X. Wang and J. Ji, *Adv. Mater.*, 2016, **28**, 8265–8270.
13 Z. Chen, T. Ming, M. M. Goulamaly, H. Yao, D. Nezich, M. Hempel, M. Hofmann and J. Kong, *Adv. Funct. Mater.*, 2016, **26**, 5061–5067.
14 Q. Shao, Z. Niu, M. Hirtz, L. Jiang, Y. Liu, Z. Wang and X. Chen, *Small*, 2014, **10**, 1466.
15 M. Xue, F. Li and T. Cao, *Nanoscale*, 2012, **4**, 1939–1947.
16 S. Gong, W. Schwalb, Y. Wang, Y. Chen, Y. Tang, J. Si, B. Shirinzadeh and W. Cheng, *Nat. Commun.*, 2014, **5**, 3132.
17 D. J. Lipomi, M. Vosgueritchian, B. C. Tee, S. L. Hellstrom, J. A. Lee, C. H. Fox and Z. Bao, *Nat. Nanotechnol.*, 2011, **6**, 788–792.
18 Q. Sun, D. H. Kim, S. S. Park, N. Y. Lee, Y. Zhang, J. H. Lee, K. Cho and J. H. Cho, *Adv. Mater.*, 2014, **26**, 4735–4740; B. Zhu, Z. Niu, H. Wang, W. R. Leow, H. Wang, Y. Li, L. Zheng, J. Wei, F. Huo and X. Chen, *Small*, 2014, **10**, 3625–3631; Y. A. Samad, Y. Li, S. M. Alhassan and K. Liao, *ACS Appl. Mater. Interfaces*, 2015, **7**, 9195–9202.
19 L. Hu, M. Pasta, F. L. Mantia, L. Cui, S. Jeong, H. D. Deshazer, J. W. Choi, S. M. Han and Y. Cui, *Nano Lett.*, 2010, **10**, 708–714.
20 B. K. Little, Y. Li, V. Cammarata, R. Broughton and G. Mills, *ACS Appl. Mater. Interfaces*, 2011, **3**, 1965–1973.

21 X. Liu, H. Chang, Y. Li, W. T. Huck and Z. Zheng, *ACS Appl. Mater. Interfaces*, 2010, **2**, 529–535.
22 C. Ye, M. Li, M. Xue, W. Shen, T. Cao, Y. Song and L. Jiang, *J. Mater. Chem.*, 2011, **21**, 5234.
23 F. Wang, M. Xue and T. Cao, *Adv. Mater.*, 2009, **21**, 2211–2215.
24 D. Zhao, L. Duan, M. Xue, W. Ni and T. Cao, *Angew. Chem., Int. Ed.*, 2009, **48**, 6699–6703.
25 X. Ma, D. Zhao, M. Xue, H. Wang and T. Cao, *Angew. Chem., Int. Ed.*, 2010, **49**, 5537–5540.
26 H. Tian, Y. Shu, X. F. Wang, M. A. Mohammad, Z. Bie, Q. Y. Xie, C. Li, W. T. Mi, Y. Yang and T. L. Ren, *Sci. Rep.*, 2015, **5**, 8603.
27 S. Lee, A. Reuveny, J. Reeder, S. Lee, H. Jin, Q. Liu, T. Yokota, T. Sekitani, T. Isoyama, Y. Abe, Z. Suo and T. Someya, *Nat. Nanotechnol.*, 2016, **11**, 472–478.
28 M. Xue, D. Chen, Y. Long, P. Wang, L. Zhao and G. Chen, *Adv. Mater.*, 2015, **27**, 3614–3619.
29 Y. Duan, Y. Huang, Z. Yin, N. Bu and W. Dong, *Nanoscale*, 2014, **6**, 3289–3295.
30 S. I. Ahn, J. Jung, Y. Kim, Y. Lee, K. Kim, S. E. Lee, S. Kim and K. K. Choi, *Sci. Rep.*, 2016, **6**, 38830.
31 M. Xue, X. Cai and G. Chen, *Small*, 2015, **11**, 548–552.
32 Z. Yang, H. Liang, X. Wang, X. Ma, T. Zhang, Y. Yang, L. Xie, D. Chen, Y. Long, J. Chen, Y. Chang, C. Yan, X. Zhang, X. Zhang, B. Ge, Z. Ren, M. Xue and G. Chen, *ACS Nano*, 2016, **10**, 755–762.
33 J. Zhu, M. Xue, D. Zhao, M. Zhang, L. Duan, Y. Qiu and T. Cao, *Angew. Chem., Int. Ed.*, 2011, **50**, 12478–12482.
34 L. Pan, A. Chortos, G. Yu, Y. Wang, S. Isaacson, R. Allen, Y. Shi, R. Dauskardt and Z. Bao, *Nat. Commun.*, 2014, **5**, 3002.
35 D. D. Kulkarni, I. Choi, S. S. Singamaneni and V. V. Tsukruk, *ACS Nano*, 2010, **4**, 4667–4676.
36 X. Xu, Z. Sun, D. H. Chua and L. Pan, *Sci. Rep.*, 2015, **5**, 11225.
37 H. Hu, Z. Zhao, W. Wan, Y. Gogotsi and J. Qiu, *Adv. Mater.*, 2013, **25**, 2219–2223.
38 H. Sun, Z. Xu and C. Gao, *Adv. Mater.*, 2013, **25**, 2554–2560.
39 C. Wang, X. Wang, Y. Wang, J. Chen, H. Zhou and Y. Huang, *Nano Energy*, 2015, **11**, 678–686.
40 S. J. Woltornist, D. Varghese, D. Massucci, Z. Cao, A. V. Dobrynin and D. H. Adamson, *Adv. Mater.*, 2017, 29.
41 Y. Zhao, J. Liu, Y. Hu, H. Cheng, C. Hu, C. Jiang, L. Jiang, A. Cao and L. Qu, *Adv. Mater.*, 2013, **25**, 591–595.
42 Z. Chen, C. Xu, C. Ma, W. Ren and H. M. Cheng, *Adv. Mater.*, 2013, **25**, 1296–1300.
43 F. Li, J. Chen, X. Wang, M. Xue and G. F. Chen, *Adv. Funct. Mater.*, 2015, **25**, 4601–4606.
44 C. Wu, X. Huang, X. Wu, R. Qian and P. Jiang, *Adv. Mater.*, 2013, **25**, 5658–5662.
45 F. Yavari, Z. Chen, A. V. Thomas, W. Ren, H. M. Cheng and N. Koratkar, *Sci. Rep.*, 2011, **1**, 166.
46 Y. Liu, H. Liang, Z. Xu, J. Xi, G. Chen, W. Gao, M. Xue and C. Gao, *ACS Nano*, 2017, **11**, 4301–4306.
47 H. Liang, X. Ma, Z. Yang, P. Wang, X. Zhang, Z. Ren, M. Xue and G. Chen, *Carbon*, 2016, **99**, 585–590.
48 H. B. Yao, J. Ge, C. F. Wang, X. Wang, W. Hu, Z. J. Zheng, Y. Ni and S. H. Yu, *Adv. Mater.*, 2013, **25**, 6692–6698.
49 Y. A. Samad, Y. Li, A. Schiffer, S. M. Alhassan and K. Liao, *Small*, 2015, **11**, 2380–2385.
50 S. Wan, H. Bi, Y. Zhou, X. Xie, S. Su, K. Yin and L. Sun, *Carbon*, 2017, **114**, 209–216.
51 L. Sheng, Y. Liang, L. Jiang, Q. Wang, T. Wei, L. Qu and Z. Fan, *Adv. Funct. Mater.*, 2015, **25**, 6545–6551.
52 M. Xue, D. Chen, X. Wang, J. Chen and G. F. Chen, *J. Mater. Chem. A*, 2015, **3**, 7715–7718.
53 C. Yan, J. Wang, W. Kang, M. Cui, X. Wang, C. Y. Foo, K. J. Chee and P. S. Lee, *Adv. Mater.*, 2014, **26**, 2022–2027.
54 F. Zhao, L. Wang, Y. Zhao, L. Qu and L. Dai, *Adv. Mater.*, 2017, **29**, 1604972.
55 U. N. Maiti, J. Lim, K. E. Lee, W. J. Lee and S. O. Kim, *Adv. Mater.*, 2014, **26**, 615–619.
56 H. Liu, H. Wang and X. Zhang, *Adv. Mater.*, 2015, **27**, 249–254.
57 Y. Qin, Q. Peng, Y. Ding, Z. Lin, C. Wang, Y. Li, F. Xu, J. Li, Y. Yuan, X. He and Y. Li, *ACS Nano*, 2015, **9**, 8933–8941.
58 Y. Pang, H. Tian, L. Tao, Y. Li, X. Wang, N. Deng, Y. Yang and T. L. Ren, *ACS Appl. Mater. Interfaces*, 2016, **8**, 26458–26462.
59 Y. Abdul Samad, Y. Li and K. Liao, *MRS Adv.*, 2016, **1**, 27–32.
60 M. Zhang, Y. Wu, X. Wang and X. Wang, *Int. J. Mod. Phys. B*, 2017, **31**, 1741009.
61 S. H. Shin, S. Ji, S. Choi, K. H. Pyo, B. Wan An, J. Park, J. Kim, J. Y. Kim, K. S. Lee, S. Y. Kwon, J. Heo, B. G. Park and J. U. Park, *Nat. Commun.*, 2017, **8**, 14950.
62 Z. Chen, Z. Wang, X. Li, Y. Lin, N. Luo, M. Long, N. Zhao and J. B. Xu, *ACS Nano*, 2017, **11**, 4507–4513.